PCCP

PAPER

View Article Online
View Journal

Check for updates

Cite this: DOI: 10.1039/d4cp04293j

Novel $Cs_2Au^{I}M^{III}F_6$ (M = As, Sb) double halide perovskites: sunlight and industrial waste heat management device applications†

Shuaib Mahmud, *[ab] Usama Ahmed,[a] Md. Atik Uz Zaman Atik,[c] Md. Mukter Hossain,[a] Md. Mohi Uddin[a] and Md. Ashraf Ali *[a]

Received 10th November 2024,
Accepted 21st January 2025

DOI: 10.1039/d4cp04293j

rsc.li/pccp

The upcoming lead-free double halide perovskites are sustainable alternatives to lead perovskites in renewable energy technologies. This study conducted a comprehensive investigation into the structural, electronic, optical, and thermoelectric properties of novel $Cs_2Au^{I}M^{III}F_6$ (M = As, Sb) double halide perovskites using a density functional theory-based approach. The tolerance factors and negative formation energies, as well as analysis of phonon dispersion, confirm structural and dynamic stability. There are favorable values of elastic coefficients and Pugh's and Poisson's ratios, which prove that there is mechanical stability, and ductility is also proven. The compounds show indirect band gaps of 1.144 eV (Cs_2AuAsF_6) and 1.746 eV (Cs_2AuSbF_6), which fall within the range of absorption of visible light. Optical analysis reveals high absorption coefficients, thereby making this material suitable for photovoltaic applications. Thermoelectric properties show moderate ZT values of approximately 0.64 and 0.61 at 500 K, which signify their application for waste heat recovery. Thus, the currently presented work proves the potential of $Cs_2Au^{I}M^{III}F_6$ (M = As, Sb) perovskites as effective materials from an environmental perspective for energy harvesting devices.

1. Introduction

The use of modern technology has greatly contributed to improving the overall quality of life for humans, leading to global economic progress. The large increase in energy consumption has thus prompted experts to step up their efforts to find alternatives to fossil fuels and other conventional sources. Current energy sources are mostly fossil fuel which poses significant environmental risks and is rapidly depleting.[1–3] Consequently, experts are now conducting thorough investigations into many renewable energy sources as a prospective surrogate for the existing energy sources.[4] Among the renewable energy sources, solar energy is particularly prevalent. Various materials are used to fabricate solar cells. Perovskite materials have exceptional properties, including a high absorption coefficient, improved carrier mobility, and better luminous performance. The characteristics of perovskite materials have propelled their progress.[5] Solar cells now use optoelectronics technology, which has garnered significant attention. Researchers have recently shown a growing interest in perovskite solar cells due to their remarkable photoelectric conversion efficiency, affordability, and simple production process.[6–8] Lead-free double halide perovskites with the capability of overcoming the toxicity and stability problems associated with the conventional lead-based perovskites have emerged as attractive materials. However, their power conversion efficiency is still low because of factors such as poor light harvesting capability and indirect band gap which are intangible characteristics of matter.[9]

Photovoltaic and thermoelectric technologies utilize two energy sources, namely sunlight and industrial waste heat, to efficiently transform light or heat into electricity. The choice of materials impacts the effectiveness of both photoelectric technology and thermal purposes. The perovskite halide materials of the form ABX_3 and A_2BX_6 (or $A_2B'B''X_6$) are known as single or double perovskites (DP). The B-site cationic charge arrangement of double perovskites (DP), consisting of B′ (monovalent) and B″ (trivalent), can accommodate 4^+, whereas single perovskites are limited to only 2^+.[10] The DPs include two octahedra, $B'X_6$ and $B''X_6$, with X positioned in the middle of both octahedra. The B′ and B″ ions are located at the corner-sharing octahedral sites, while the spaces between the two octahedral Cs ions are occupied by interstitial ions in the 3D structure.[11]

---

[a] Advanced Computational Materials Research Laboratory, Department of Physics, Chittagong University of Engineering and Technology (CUET), Chattogram-4349, Bangladesh. E-mail: shuaib.eee.iu@gmail.com, ashrafphy31@cuet.ac.bd

[b] Department of Electrical and Electronic Engineering, Jatiya Kabi Kazi Nazrul Islam University (JKKNIU), Mymensingh-2224, Bangladesh

[c] Department of Electrical and Electronic Engineering, Atish Dipankar University of Science and Technology (ADUST), Dhaka-1230, Bangladesh

† Electronic supplementary information (ESI) available. See DOI: https://doi.org/10.1039/d4cp04293j

These types of lead-based DPs show a light conversion efficiency of about 20%,[12,13] but stability is the main issue. Despite this great productivity, Pb would need to be replaced by less toxic and less expensive materials for a healthy environment. In order to do this, DP halides have been studied and synthesized using lead-free substances.[14,15] Furthermore, it is becoming more apparent that the ability of DPs to be composed in different ways allows for a range of capabilities to improve the properties of the material. This leads to enhanced performance in modern electronic applications and energy-related technologies, such as opto-electronics,[16,17] catalysis,[18,19] magnetism,[20,21] and the production of electricity.[22–25]

Recently, there has been extensive research into the possibility of novel lead-free inorganic double perovskite materials containing halides for use in solar applications.[16,26] Double halide perovskites (A_2SeX_6; A = Rb, K; X = Cl, Br, I), compounds with an indirect band gap in the visible light range, are suitable for renewable energy devices and applications.[25] M. A. Ali *et al.* demonstrated that the new double perovskites K_2AgAsX_6 (X = Cl, Br) possess significant band gaps (2.10, 1.48 eV) and lower carrier mass, rendering them appropriate for use as absorber layers in solar cells.[26] Researchers are investigating halide perovskite materials for their ideal physical features for energy-related applications. We expect these materials to significantly contribute to the generation of renewable energy. S. Mahmud *et al.* utilized the full potential linearized augmented plane wave method within the density functional theory to determine the optical, electronic, structural, thermoelectric, and elastic properties of Cs_2AuScX_6 (X = Cl, Br, and I).[27] They discovered that this compound exhibits an indirect visible range band gap (1.88, 1.68, and 1.30 eV) and possesses a combination of ionic and covalent bonding. According to the findings of research conducted by Lozhkina and colleagues, $Cs_2BiAgBr_6$ was found to be an indirect band gap compound with an energy of 1.728 eV.[28] Mathew *et al.* suggested using $Cs_2AgInCl_6$ (with an energy gap of 1.1 eV) for its favorable optoelectronic characteristics.[29] Nazir *et al.* investigated the impact of substituting anions in Rb_2AgAsZ_6 (Z = Cl, Br, and I) on enhancing their thermoelectric and solar cell properties. They determined the band gaps of $Rb_2AgAsCl_6$, $Rb_2AgAsBr_6$, and Rb_2AgAsI_6 to be 2.21, 1.50, and 0.52 eV, respectively.[30] Mustafa *et al.* explored the properties of K_2YAgX_6 (X = Br, I) and discovered an increasing pattern in the refractive index, reflectivity, and dielectric constant as I replaces Br. The potential of these materials for optoelectronic and thermoelectric devices is demonstrated by estimating several thermoelectric parameters, such as the power factor and figure of merit, using the semi-classical Boltzmann theory-based BoltzTraP code.[31] Ayyaz *et al.* also calculated temperature-dependent thermodynamic parameters of Rb_2TlBiZ_6 by using the BoltzTraP algorithm and found a significant relationship between high electrical conductivity and poor thermal conductivity. These DPs have good prospects for potential future uses in power production from light and waste heat, as shown by a higher Seebeck coefficient combined with *ZT*.[32] Al-Qaisi *et al.* performed a study on Na_2CuMCl_6 (M = Bi, Sb) double-halide perovskites and discovered that these compounds are semiconductors with a tiny band gap. They also observed that these materials had high absorption, excellent conductivity, and low reflectivity.[33] The prospective applications revealed by the previous literature stimulated us to deal with double perovskite halides. For these reasons, we aimed to discover some potential double perovskites for the applications mentioned above.

Concurrent with photovoltaics, thermoelectric (TE) technology has garnered much interest in recent decades for its ability to turn waste heat into electrical power. Materials with low thermal conductivity but high electrical conductivity and high Seebeck coefficient, and with a figure of merit (*ZT*) value of about 1, appear to be excellent TE materials.[34] The significance of the fact that double-halide perovskite materials have low thermal conductivity due to their cation structure has led to only limited experimental attention toward their thermoelectric (TE) efficiency. In contrast, optoelectronic applications are the ones that make best use of these types of materials. Despite this, people are becoming more interested in TE properties because theoretical research shows that a number of perovskite materials, like Cs_2AuScI_6 (ZT = 0.62)[27] and Cs/Rb_2AuYI_6 (ZT = 0.62, 0.75),[35] have a *ZT* value close to 1. A recent study by A. Boutramine *et al.* investigated lead-free halide perovskites and reported a *ZT* value of 0.99 (without lattice contribution) for Rb_2CuMF_6 (M = As^{3+}, Bi^{3+}) at ambient temperature, suggesting potential applications in useful energy production devices.[36]

Therefore, the aforementioned literature promotes the use of various B-site cationic elements ($Au^{1+}As^{3+}$ and $Au^{1+}Sb^{3+}$) combined with halides for massive energy production. There are no existing studies that provide theoretical or experimental evidence. Hence, we used density functional theory (DFT) to analyze the stability, electronic and thermoelectric transport data, optical characteristics, and thermo-mechanical properties of $Cs_2Au^{I}M^{III}F_6$ (M = As, Sb) double halide perovskites. Their small band gap inspired us to study the most desired energy related device application.

2. Computational technique

The Wien2k code was used to compute various physical parameters within the framework of density functional theory (DFT).[37] This technique is based on the full potential linearized augmented plane wave (FP-LAPW) approach, which expands the electronic wave function.[38] The unit cell is separated by the LAPW technique into two regions: muffin tin radius (or atomic spheres), where wave functions are enlarged, and interstitial, where plane waves are utilized. The titled compounds were optimized for structural attributes in their ground state by solving the Kohn–Sham equation using the GGA–PBE (generalized gradient approximation of Perdew–Burke–Ernzerhof) exchange–correlation functional technique.[39] The SCF iteration is executed until convergence is attained by updating the charge density and solving for a new wave function *via* the calculation of an effective potential.[40] To achieve this, we must set up the basis parameter as follows: *k* points (13 × 13 × 13), charge convergence (ce) = 0.0001e, energy convergence (ec) = 10^{-5} Ry, $R_{\mathrm{MT}} \times K_{\max} = 8$ (R_{MT} values for Cs_2AuAsF_6 elements are Cs = 2.5, Au = 2.24, As = 2.13, F = 1.93 and for Cs_2AuSbF_6 elements are Cs = 2.5, Au = 2.3, Sb = 2.25, F = 1.98), $G_{\max} = 12$, and $I_{\max} = 10$, where R_{MT}, $G_{\max}$, and $I_{\max}$ denote muffin tin radius, Gaussian parameter, and angular momentum, respectively. We used a more sophisticated TB-mBJ (Tran-Blaha modified Becke–Johnson) functional to calculate the band structure and transport characteristics, including optoelectronic and TE properties.[41] This approach is not only efficient in terms of time but also yields results that nearly matching HSE-06 functional data.[42] High-density k points of 6000 and 12 000 were used for the DOS and optical characteristics, respectively. The thermoelectric transport parameter was computed using Boltzmann's theory using the Boltztrap2 tool.[43] The second order derivatives cubic-elastic package was used to calculate the elastic constant and thermo-physical properties.[44] We also used the CASTEP algorithm to determine the dynamic stability, namely the phonon dispersion, using the finite displacement approach.[45]

3. Results and discussion

3.1 Structural properties with stability

The compound Cs_2AuMF_6 (M = As, Sb) forms crystals with a cubic double perovskite structure that belongs to the $Fm\bar{3}m$ space group (#225) as shown in Fig. 1. Two Cs^+ cations occupy the large A-sites in the unit cell, while Au^+ and M^{3+} (M = As^{3+}, Sb^{3+}) cations are statistically distributed over the smaller B′ and B″ sites, corresponding to the chemical formula A_2BX_6. These B-cations (average of B′ and B″) are surrounded by six F-anions, arranged in the shape of octahedra. This structure forms a large cubic box with Cs^+ ions at each corner, Au^+ and M^{3+} ions alternating within the box's body, and F-ions surrounding these central cations to stabilize the crystal structure.[46]

Firstly, we optimized the unit cell using the GGA–PBE functional method and provided the minimum energy, known as ground state energy, relative to its volume. In our current work, the lowest energy state of a unit cell is used as the most stable condition to predict the physical properties. For Cs_2AuAsF_6, the volume, V = 1289.53 bohr^3, minimizes the overall energy at $E_0 = -74\,978.27$ Ry. Furthermore, the values $E_0 = -83\,423.46$ Ry and V = 1396.16 bohr^3 indicate the lowest levels of total energy for Cs_2AuSbF_6. These optimizations (E–V) are obtained by fitting the Birch–Murnaghan equation of state,[47] as shown in Fig. S1 (ESI†). The computed lattice parameter is increased from 9.1432 to 9.3886 Å as the size of the M (= As, Sb) atom goes up.

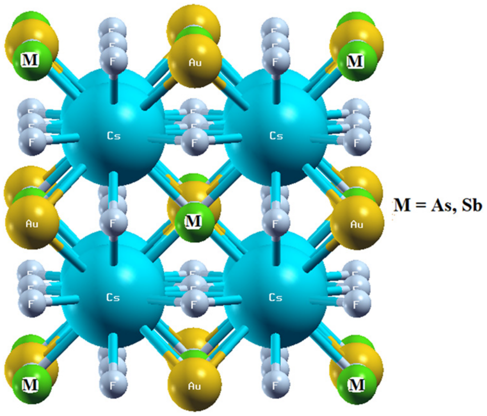

Fig. 1 Optimized unit cell of Cs_2AuMF_6 (M = As, Sb) [3D structure].

Prior to conducting full research on other physical and optoelectronic features, it is crucial to conduct a comprehensive investigation into the stability of the materials in order to determine their suitability for practical use. The structural cubic stability of Cs_2AuMF_6 (M = As, Sb) is estimated using Goldschmidt's tolerance factor (T_F) and octahedral factor (μ) with the following parameters:[48,49]

$$T_F = \frac{R_{Cs} + R_F}{\sqrt{2}\left(\dfrac{R_{B'} + R_{B''}}{2} + R_F\right)}$$

$$\mu = \frac{R_{B'} + R_{B''}}{2R_F}$$

The following equation, which was introduced by C. J. Bartel *et al.*, provides a new tolerance factor with a 91% accuracy rate for predicting the structural integrity of DP halide materials:[50]

$$\tau = \frac{2R_F}{R_{B'} + R_{B''}} - n_A\left[n_A - \left(\frac{2R_A}{R_{B'} + R_{B''}}\right)\Big/\ln\left(\frac{2R_A}{R_{B'} + R_{B''}}\right)\right]$$

where R_{Cs} stands for the radius of alkali ions (Cs), R_B for the radius of B-site ions ($R_{B'}$ for Au and $R_{B''}$ for M) and R_F for the radius of halogen F. Shannon's ion radii are used here to determine these factors.[51] The values of T_F decrease due to the increasing size of the atoms of As and Sb. A T_F value ranging from 0.81 to 1.10 typically suggests the presence of a stable perovskite structure.[52] The octahedral factors also fit within the range that is appropriate for a cubic structure, which is $0.38 < \mu < 0.90$.[53] The Goldschmidt tolerance factor is appropriate for predicting the stability of simpler perovskites but it poses difficulties when extended to a more complex system like a double perovskite, where the presence of other parameters like electronic arrangement and local coordination becomes more significant.

In order to improve the evaluation of the stability of these double perovskites, we applied the modified tolerance factor which considers the peculiar structural and electronic features of Cs_2AuMF_6 compounds. The factor extends the traditional considerations of the ionic size compatibility predictability by adding further parameters to be more in line with the experimental observations on stability. The new tolerance factor range, denoted as $\tau < 4.18$, and the compounds used in this investigation meet the ranges under ambient conditions which are listed in Table 1. So, these double perovskite compounds under investigation are stable. Furthermore, T_F drops from As to Sb, providing additional evidence that the comparative analysis shows that Cs_2AuAsF_6 is more stable than Cs_2AuSbF_6.

Table 1 Structural parameters and stability of Cs_2AuAsF_6 and Cs_2AuSbF_6 compounds

Parameter	Cs_2AuAsF_6	Cs_2AuSbF_6
Lattice constant $a = b = c$ (Å)	9.1432	9.3886
Tolerance factor, T_F	0.98	0.95
New tolerance factor (physically based), τ	3.29	3.34
Octahedral factor, μ	0.73	0.80
Formation energy, ΔH_f (eV)	−3.21	−3.07

To further demonstrate stability, we have calculated the formation energy of compounds under study using the following equation:[54]

$$\Delta H_f = [E_{Cs_2AuMF_6} - (8E_{Cs} + 4E_{Au} + 4E_M + 24E_F)]/40$$

where $E_{Cs_2AuMF_6}$ denotes the compound's total energy and E_{Cs}, E_{Au}, E_M, and E_F are the energies of the Cs, Au, M, and F atoms, respectively. Table 1 also presents the titled compounds, which exhibit negative formation energy, confirming the structural stability.

Fig. 2 displays the phonon dispersion curve (PDC) with the total and partial density of states (DOS) of the compounds. Two distinct modes, acoustic and optic, compose the dispersion curve. This composition exhibits a total of 30 vibrational modes in a primitive cell. This is due to the presence of 10 atoms per unit cell within the framework of the CASTEP code. The acoustic mode converges towards the gamma point and functions at lower frequencies, whereas the optic mode acts within the higher frequency range. The partial density of states (PDOS) provides insights into the distinct contributions of individual atoms or atom groups to the vibrational modes, whereas the total density of states (TDOS) characterizes the overall distribution of vibrational frequencies in the material. In the composites of Cs_2AuMF_6 (M = As, Sb), the halide atom F mostly contributes in the high-frequency band, while Cs and Au (heavy atom) contribute in the low-frequency ranges. It is crucial to emphasize that phonon calculations indicate that the presence of positive frequencies in the vibrational modes of atoms indicates a dynamically stable structure for all the studied materials at zero pressure.

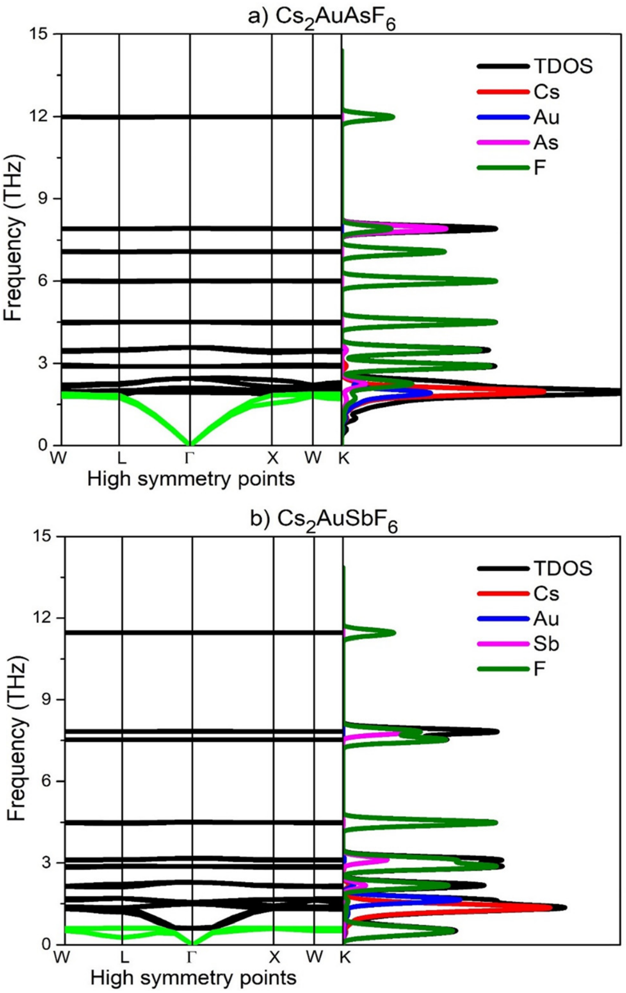

Fig. 2 Phonon dispersion with total (TDOS) and partial density of states (PDOS) of (a) Cs_2AuAsF_6 and (b) Cs_2AuSbF_6.

3.2. Electronic properties, effective mass of charge carriers, exciton binding energy and density of states (DOS)

The electronic properties of materials determine the mechanisms of carrier transport, enabling the differentiation between metals, semimetals, semiconductors, and insulators. The energy band gaps within the energy range of +6 eV to −6 eV obtained from the calculations are displayed in Fig. 3. The band structures of the computed materials exhibit similarity and are all classified as indirect, as the valence band maximum (VBM) is situated at the X point, while the conduction band minimum (CBM) is situated at the L point. The band gap energy values for Cs_2AuAsF_6 and Cs_2AuSbF_6 are 1.144 eV and 1.746 eV, respectively, by the TB-mBJ approach. In addition, the compounds provide low band gap energy values of 0.518 eV and 0.777 eV for Cs_2AuAsF_6 and Cs_2AuSbF_6, respectively, when calculated with GGA–PBE. Since electrons in an indirect band gap require phonon help to go from the valence band to the conduction band, they usually have a lower photon absorption efficiency than in a direct band gap. However, the determined band gap values imply that these substances have the ability to absorb visible spectrum photons, which is necessary for solar energy harvesting. The TB-mBJ approximation was chosen in this work due to its high precision in determining the band gap compared to the GGA–PBE approximation. The TB-mBJ approach yielded values that closely aligned with the band gap predicted by the experiment.[41] The TB-mBJ + SOC method was also applied in the study; as there were negligible differences (±0.03) the graphs were not shown. Consequently, because of their perfectly positioned band gaps for efficient light absorption and energy conversion, Cs_2AuAsF_6 and Cs_2AuSbF_6 are attractive options for optoelectronic applications, such as absorber layers in solar cells.[55]

The effective mass of charge carriers in double perovskite materials indicates the resistance of charge carriers, such as electrons or holes, within the crystal lattice of the material. Charge carriers with a smaller effective mass are more responsive to an applied electric field, which leads to increased efficiency in charge transport and energy conversion. By evaluating the second derivatives of energy (E) with respect to

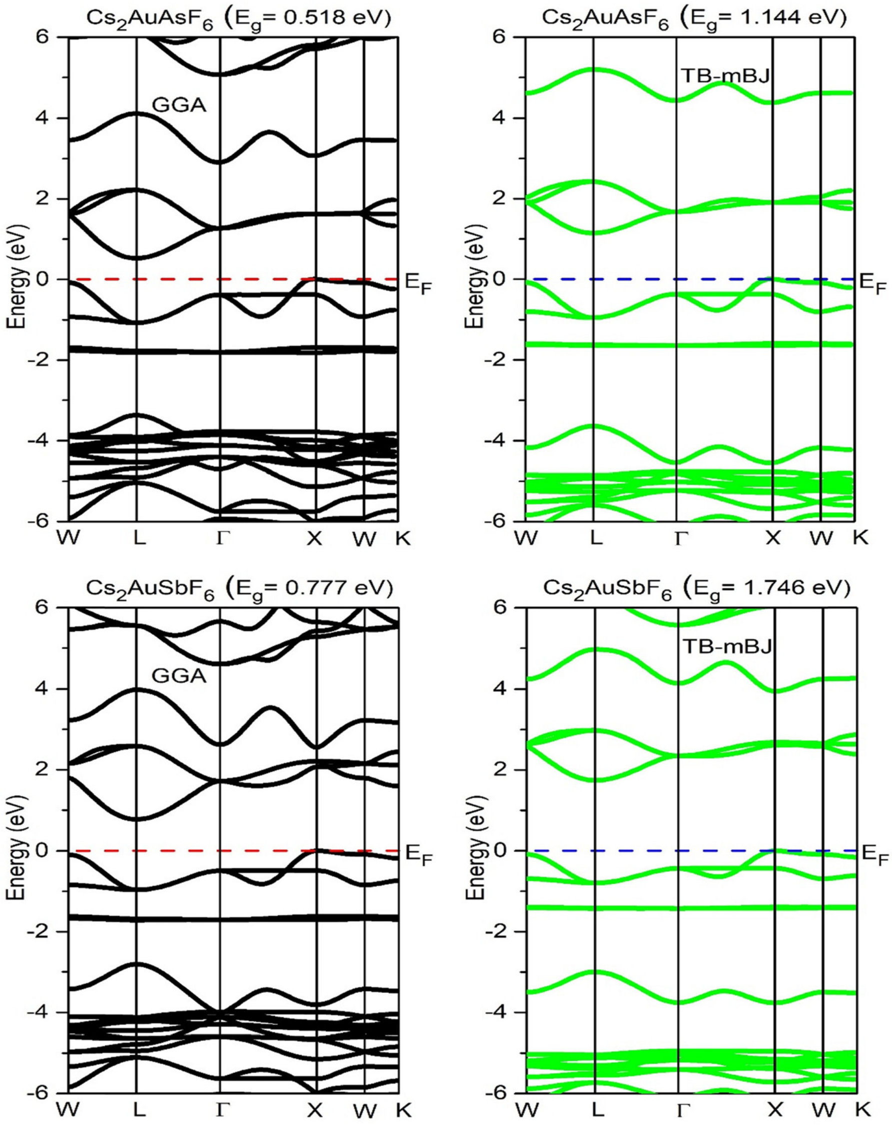

Fig. 3 Band diagram of Cs_2AuAsF_6 and Cs_2AuSbF_6, calculated using the GGA–PBE (left side) and TB-mBJ (right side) techniques.

momentum (K), which represent the curvature of the band edges, we can determine the effective mass using the following relation:[56]

$$\frac{1}{m^*} = \frac{1}{\hbar^2}\frac{\mathrm{d}^2E}{\mathrm{d}K^2}$$

A low effective mass has the potential to lead to an increase in carrier mobility. An inquiry into the charge carriers (electrons and holes) in double perovskite materials is crucial for understanding their electrical properties. The studied materials allow for the fast and unimpeded passage of electrons because of their low effective electron mass (0.16 for Cs_2AuAsF_6 and 0.25 for Cs_2AuSbF_6). The materials investigated also demonstrate promise for use in optoelectronic devices as a result of their suitable band gaps and high absorption in the visible spectrum (Cs_2AuAsF_6 exhibits stronger absorption compared to Cs_2AuSbF_6), which are critical for effective photon capture and excitation of electrons.

The exciton binding energy (E_b^ex) is a key parameter that influences the performance of materials in solar cell applications. For efficient charge separation, this energy needs to be low. This allows the excitons (bound electron–hole pairs) to dissociate into free carriers (electrons and holes) more easily under thermal energy at room temperature. If the exciton binding energy is too high, excitons may not dissociate efficiently, resulting in lower charge carrier mobility and higher recombination rates, which negatively impact the solar cell's performance. The photo-excited electron–hole coulomb interaction causes excitonic phenomena. E_b^ex is calculated by the Wannier–Mott exciton model with the high dielectric constant of Cs_2AuAsF_6 and Cs_2AuSbF_6 double perovskite semiconductors using the following relation:[57]

$$E_\mathrm{b}^\mathrm{ex} = \frac{\mu_\mathrm{r}e^4}{32(\pi\varepsilon_0\hbar^2\varepsilon_\mathrm{r})^2} = 13.56\frac{\mu_\mathrm{r}}{m_\mathrm{e}\varepsilon_1(0)^2} \quad \text{where,}\ \mu_\mathrm{r} = \frac{m_\mathrm{e}^* \times m_\mathrm{h}^*}{m_\mathrm{e}^* + m_\mathrm{h}^*}$$

Table 2 Computed band gaps and effective mass of charge carriers for investigated compounds

	Band gap (eV)			Effective mass by TB-mBJ		Exciton binding energy
Compound	GGA–PBE	TB-mBJ	Nature	m_h^*/m_0	m_e^*/m_0	E_b^{ex}
Cs_2AuAsF_6	0.518	1.144	Indirect	0.48	0.16	0.44
Cs_2AuSbF_6	0.777	1.746	Indirect	0.72	0.25	1.12

where e is the elementary charge, ε_0 is the vacuum permittivity, $\hbar$ is the reduced Planck constant, ε_r is the relative permittivity (dielectric constant) of the material, and μ_r is the reduced mass of the electron–hole pair. A low exciton binding energy of Cs_2AuAsF_6 compared to Cs_2AuSbF_6 in Table 2 ensures optimal light absorption and charge transport, contributing to the overall stability and performance of the solar cell. Therefore, we suggest these materials as an appropriate choice for solar cell applications functioning in the visible light regions of the electromagnetic spectrum.

In addition, Fig. 4 depicts the distribution of electrons in Cs_2AuAsF_6 and Cs_2AuSbF_6 through a graph that presents the overall and partial density of states (DOS). The band structure and the total density of states (DOS) exhibit identical patterns. In general, density of states (DOS) illustrates the various energy levels that contribute to the development of a band, with a specific focus on the material's transport capabilities. The distinctions observed in band gaps in the range observed between Cs_2AuAsF_6 and Cs_2AuSbF_6 (1.144 eV *vs.* 1.746 eV) could be linked to the peculiar electronic configuration and the atomic size of Sb and As in relation to Au. The larger atomic radius in terms of dimensions of Sb will lead to reduced orbital overlap with the Au-d and F-p states, thus giving rise to an increase in the distance between the VBM and CBM. In contrast to Sb, the reduced size of As favors greater orbital hybridization, lead to narrower band gaps.

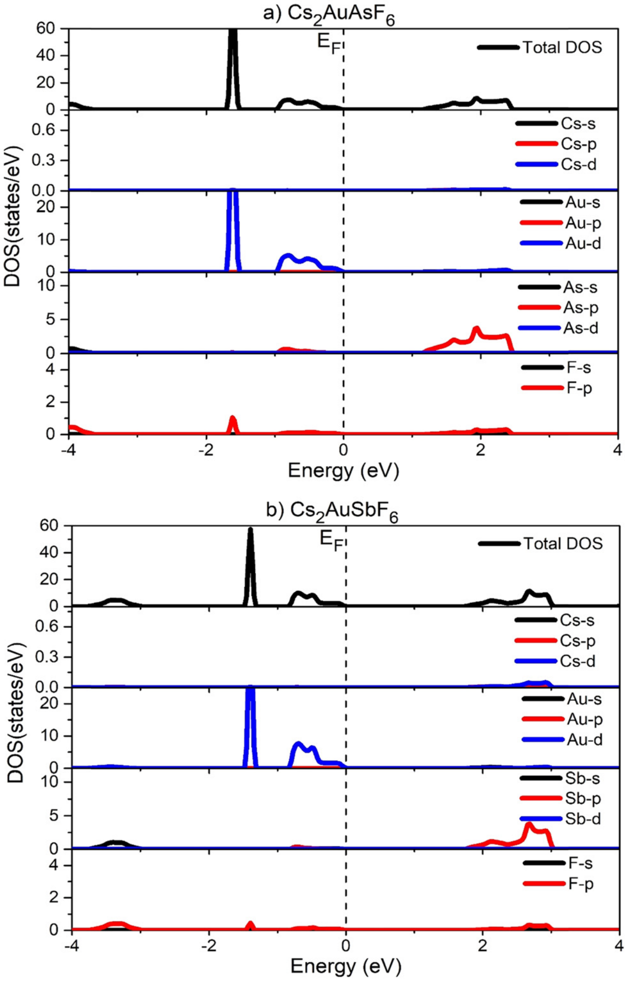

Fig. 4 Total DOS and partial DOS of investigated compounds of (a) Cs_2AuAsF_6 and (b) Cs_2AuSbF_6.

3.3. Charge density mapping

The process of charge density mapping in materials such as Cs_2AuAsF_6 and Cs_2AuSbF_6 double perovskites involves analyzing the spatial arrangement of electronic charge inside the crystal lattice. Analyzing the electron density maps can reveal the type of bonding between atoms and possible functional properties. Lower electron density areas may imply an ionic nature, whereas higher electron density regions between atoms indicate covalent bonding. The charge density maps of Cs_2AuAsF_6 and Cs_2AuSbF_6 (Fig. 5) show how the electrons are spread out among the Cs, Au, As/Sb, and F atoms.

According to charge density mapping, the As–F bond has a somewhat greater covalent character as compared with the Sb–F bond as denoted by increased electron localization around the As atom. This increased bonding strength accounts for the relatively greater stability of Cs_2AuAsF_6 manifested in a more negative formation energy than Cs_2AuSbF_6. This is because of the increased bonding strength itself. Cs^+ ions have a low electron density because they are big and normally donate

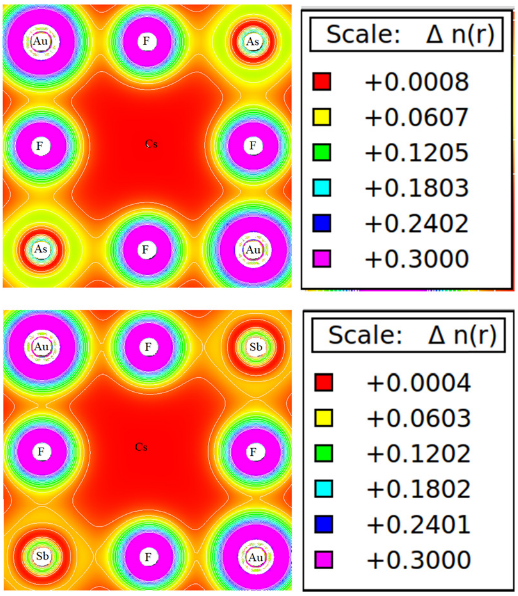

Fig. 5 Charge density mapping of Cs_2AuAsF_6 and Cs_2AuSbF_6 (2D view).

electrons rather than share them. Au^+ ions have a larger electron density surrounding them, suggesting a stronger electron attraction, whereas As^{3+}/Sb^{3+} have a lower electron density than Au^+, reflecting their participation in bond formation with F. The significant electron density of Au–F suggests a strong covalent character, and As/Sb–F also shows covalent bonding with an ionic character. These interactions along with low effective mass (0.16 for Cs_2AuAsF_6 and 0.25 for Cs_2AuSbF_6) are favorable for high electron mobility and efficient charge transfer making the compounds appropriate for optoelectronic and thermoelectric applications. Literature reports yielded similar results.[58,59] The bonding nature of Cs–F atoms has an ionic character due to large differences in electronegativity or more localized density around the Cs atom.

The spatial arrangement of charge density may have a significant effect on the electronic properties of a material. Specifically, regions with a high concentration of electrons can affect the structure of energy bands and, as a result, the conductivity of the material. Additionally, the charge density variations in perovskites of this kind may also impact the material's interaction with light, which is essential for optoelectronic applications. Therefore, charge density mapping of the studied double perovskite halide materials provides precise insights into the electronic distribution of ionic and covalent characters within the crystal structure. This information is crucial for understanding their functional characteristics.

3.4. Optical properties

The optical characteristics of a material, specifically those related to light absorption and emission, are critical in assessing its viability for optoelectronic and photovoltaic applications because they provide valuable information about the material's ability to interact with light. In order to determine the suitability of a material for optoelectronic applications, it is crucial to have a thorough knowledge of its electronic configuration and optical characteristics. The TB-mBJ approximation was used to determine the optical properties. Fig. 6(a)–(d) and 7(a)–(d) displays the optical properties of Cs_2AuMF_6 (M = As, Sb) for photon energies ranging from 0 to 6 eV.

The dielectric function is essential for comprehending the light-harvesting characteristics of double perovskite materials. The typical expression of the complex dielectric function is

$$\varepsilon(\omega) = \varepsilon_1(\omega) + i\varepsilon_2(\omega)$$

where ω represents the angular frequency of the incident light. The real part of the dielectric function is denoted as $\varepsilon_1(\omega)$,

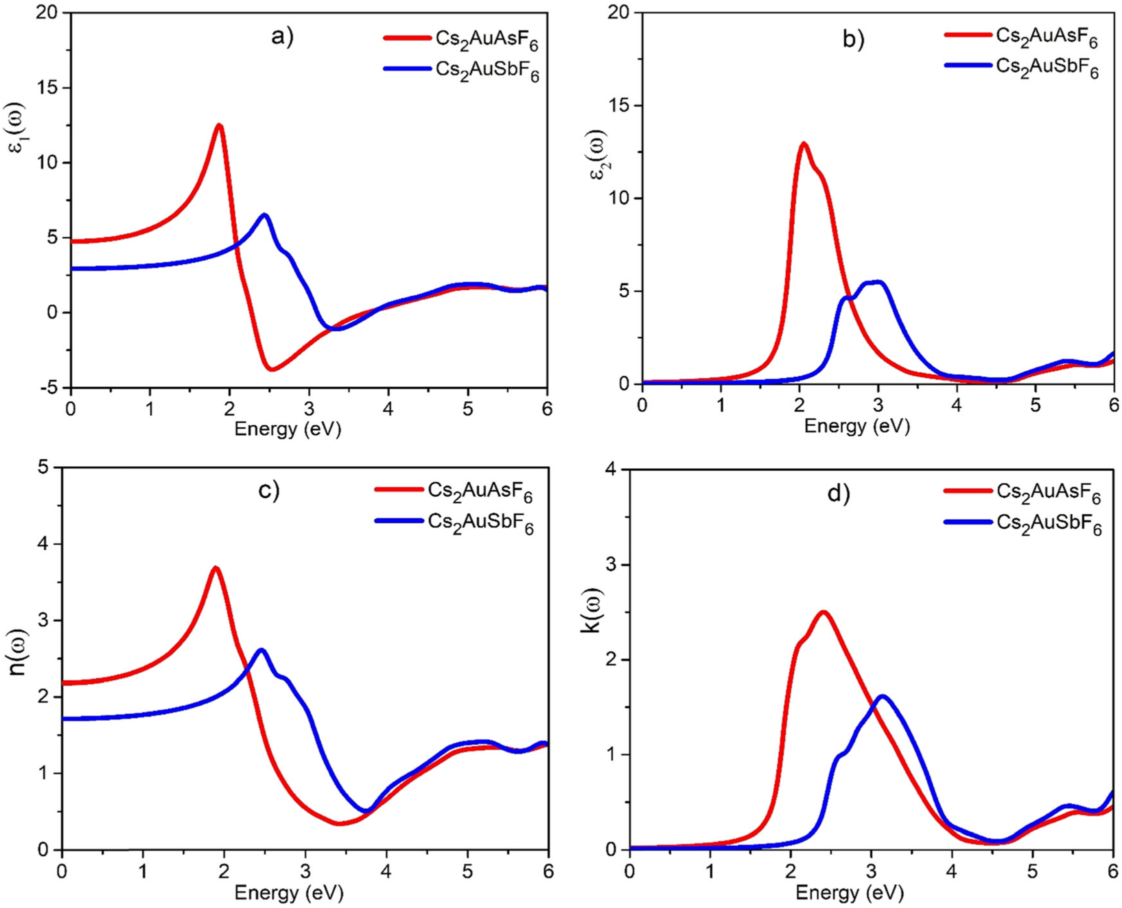

Fig. 6 (a) $\varepsilon_1(\omega)$: real part of the dielectric constant, (b) $\varepsilon_2(\omega)$:imaginary part of the dielectric constant, (c) $n(\omega)$: refractive index and (d) $k(\omega)$: extinction coefficient for studied compounds.

which describes the material's ability to store electrical energy within its structure, hence determining its refractive characteristics, and the imaginary part of the dielectric function is denoted as $\varepsilon_2(\omega)$, which describes the electronic transition features of the band structure (energy loss, absorption) at various photon energies, as presented in Fig. 6(a) and (b). Collectively, they provide a thorough depiction of the visual characteristics of a substance and are determined through the utilization of Kramer's Kronig relation.[60]

The static values $\varepsilon_1(0)$ of Cs_2AuAsF_6 and Cs_2AuSbF_6 are 4.78 and 2.98, respectively, indicate a significant polarization response, serving as a key building block in light harvesting. When the photon energy (eV) increases, the value of $\varepsilon_1(\omega)$ reaches its peak; thereafter, it starts to decline. The peak sees a downward shift as the B-site cations transition from As to Sb. The highest peaks of $\varepsilon_1(\omega)$ are 12.55 and 6.55 in the visible ranges at 1.85 eV and 2.44 eV for Cs_2AuAsF_6 and Cs_2AuSbF_6, respectively. It is crucial to highlight that due to its small band gap, Cs_2AuAsF_6 has a higher peak value in the visible spectrum (VIS) compared to Cs_2AuSbF_6. Consequently, polarized electrons may generally move more easily through Cs_2AuAsF_6 into conducting states, increasing the material's PV conversion efficiency. An empirical method for describing a semiconductor's dielectric function is the Penn model. The use of approximations like the nearly free electron model removes the complexity related to scattering processes inside a semiconductor. Because the dielectric constant, a crucial metric required to investigate how materials interact with electromagnetic radiation, can be calculated, this improves our understanding of how semiconductors behave in terms of their optical characteristics and electrical structure.[61] The values described earlier support Penn's model, which is[62]

$$\varepsilon_1(0) \approx 1 + \left[\frac{\hbar\omega_p}{E_g}\right]^2$$

However, at elevated energy levels, it undergoes a shift towards negative values, indicating the presence of metallic properties as a result of electron transitions.[63]

$\varepsilon_2(\omega)$ especially covers the energy level range of 1–3.5 eV which shows an intense tendency to absorb photons in the visible range of the electromagnetic spectrum with higher dielectric function values of 12.95 and 5.50 for Cs_2AuAsF_6 and Cs_2AuSbF_6, respectively. The DP compound's strong dielectric performance for solar energy makes it a viable option for photovoltaic technology.

The correlation between the velocity of light and the density of matter is determined by the refractive index, denoted by the symbol $n(\omega)$. Fig. 6(c) shows the refractive index $n(\omega)$. The static refractive index $n(0)$ values for Cs_2AuAsF_6 and Cs_2AuSbF_6 are 2.17 and 1.71, respectively, falling in the desirable range for efficient transmission and conversion of light in optoelectronic applications. Strong interaction with visible light is indicated by a high refractive index in Cs_2AuMF_6 compounds, which improves the material's capacity to slow down and confine light inside its crystal structure. Because it directly affects the effectiveness of photon absorption and light trapping in solar cell devices, this feature is essential for optoelectronic applications. High refractive index materials can increase light absorption in photovoltaic applications by giving photons more chances to interact with the material, which raises conversion efficiency. Optoelectronic activities need $n(\omega)$ values ranging from 2.0 to 4.0,[64] which the investigated materials satisfy, exceeding that of silicon nitride (1.9) used in solar cells[65] with comparing Cs_2AuAsF_6. In addition, compared to optical waveguide materials like silica glass, quartz, soda-lime glass, periclase, and spinel, the $n(0)$ values of both compounds are much larger. Both the functions $n(\omega)$ and $\varepsilon_1(\omega)$ exhibit a remarkably similar pattern, as follows: $\varepsilon_1(0) = n^2(0)$. Fig. 6(d) illustrates a graphical representation of the extinction coefficient $k(\omega)$, which is associated with the absorption of light. This graph exhibits a similar pattern to $\varepsilon_2(\omega)$.

One useful criterion for the optical characterization of optoelectronic materials is the optical absorption coefficient. The optical absorption coefficient, $I(\omega)$, determines the efficiency of solar power conversion and the amount of light at a specific wavelength that will be absorbed per unit length of the optical medium. Therefore, a material responds more favorably to the electron transitions from valence bands to conduction bands at a higher $I(\omega)$. The equation for the absorption coefficient, $I(\omega)$, is as follows:[66]

$$I(\omega) = \sqrt{2}\left[\sqrt{\varepsilon_1(\omega)^2 + \varepsilon_2(\omega)^2} - \varepsilon_1(\omega)\right]^{1/2}$$

Fig. 7(a) reveals that the maximum absorption coefficients of Cs_2AuAsF_6 and Cs_2AuSbF_6 are 6.17×10^5 cm^{-1} at 2.44 eV and 5.17×10^5 cm^{-1} at 3.16 eV, respectively. When B-site cations (M = As, Sb) are replaced with Sb instead of As the maximum absorption coefficient decreases, which is in the visible light region, suggesting their potential for being better solar absorbers instead of Pb-halide perovskites. These values of the absorption coefficient indicate a substantial absorption of photons in the visible light spectrum, and thus possible utilization of materials in light-harvesting applications. The absorption coefficient gives an understanding of the capabilities of a material to absorb light across different energy levels. The findings are in better agreement with the characteristics of commercially used solar cell materials such as silicon (Si) and gallium arsenide (GaAs).[67] Compared to Cs_2AuSbF_6, Cs_2AuAsF_6 exhibits stronger visible light absorption and is hence more appropriate for use in optoelectronics and photovoltaic solar cells.

Another important aspect of absorption is illustrated by optical conductivity $\sigma(\omega)$, which regulates the motion of electrons in optical materials as a result of the interaction between light and matter. Fig. 7(b) shows the graphical illustration of $\sigma(\omega)$, which has an almost similar pattern to $\alpha(\omega)$. This is because there's a direct correlation between the amount of energy absorbed and the quantity of excited electrons, resulting in a rise in $\sigma(\omega)$. In the visible light region, both Cs_2AuAsF_6 and Cs_2AuSbF_6 exhibit the highest conductivity values facilitating the generation of charge carriers under illumination. This characteristic is essential for

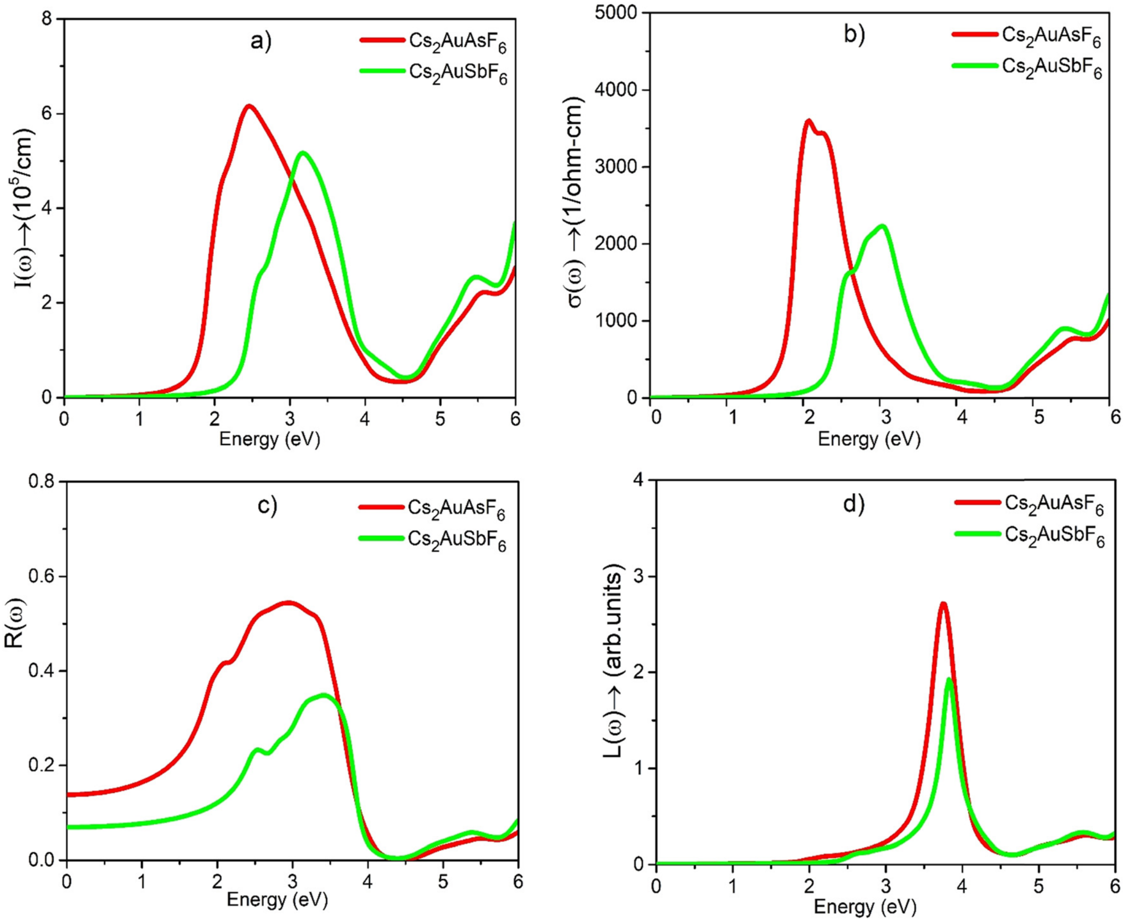

Fig. 7 (a) $I(\omega)$: absorption coefficient, (b) $\sigma(\omega)$: real optical conductivity, (c) $R(\omega)$: optical reflectivity, and (d) E_{loss}: electron energy loss of the studied compounds.

systems that use both light and electricity, such as photo-sensors and solar panels, because it shows how well the material can transform incoming radiation into electrical energy. Additionally, the higher optical conductivity implies a lower likelihood of reflection losses, which promotes appropriate energy propagation inside the apparatus.

Optical reflectivity $R(\omega)$ is a measure of the proportion of the reflected wavelengths to the incident wavelengths, which assesses the material's capacity to reflect photons that come into contact with its surface. The complete spectrum of light energy has three fundamental elements: absorption, transmission, and reflection. Fig. 7(c) depicts the measurements of light energy reflection $R(\omega)$. Table 3 presents the $R(0)$ values in a descending trend from As to Sb, indicating extremely low reflection values (less than 15%). However, within the visible spectrum (VIS), Cs_2AuAsF_6 has the ability to reflect up to 54.41% of light, whereas Cs_2AuSbF_6 can only reflect a maximum of 34.71%. Additionally, it is worth noting that Cs_2AuAsF_6 and Cs_2AuSbF_6 exhibit a significant decrease in reflectance, measuring 18.19% and 10.46%, respectively, in accordance with their band gaps. Thus, the present deposition techniques are appropriate for photovoltaic solar cells operating in the visible spectrum.

When light interacts with materials, it loses some of its energy due to scattering, material heating and thermal agitation. It is termed the loss function $L(\omega)$. This loss function is depicted in Fig. 7(d), with its values exhibiting peaks that are located away from the working or visible range. The comprehensive examination of the entire optical spectrum promises optimal absorption and slight energy loss (less than 1%) in the visible area, rendering the examined compounds very suitable for photovoltaic applications.

It should be noted that the optical properties presented here do not fully account for plasmon effects owing to the limitations of the Wien2k package, which is without GW calculation.

Table 3 Computed optical constants of studied materials

Compound	$\varepsilon_1(0)$	Maximum $\varepsilon_1(\omega)$ at eV	$n(0)$	Maximum $n(\omega)$ at eV	$I_{\max}(\omega) \times 10^5\ \text{cm}^{-1}$ at eV	$R(0)$
Cs_2AuAsF_6	4.78	12.60 at 1.86 eV	2.17	3.69 at 1.90 eV	6.17 at 2.44 eV	0.14
Cs_2AuSbF_6	2.98	6.47 at 2.42 eV	1.71	2.60 at 2.45 eV	5.17 at 3.16 eV	0.06

The contribution from plasmons is expected to be lower, as their absorption enhancement occurs primarily at higher photon energies. However, that doesn't mean we can't make use of the results, because TB-mBJ does give a good outcome for the band gap values and low-to-medium (0–6 eV) energy optical transitions. The conclusions drawn up here are thus valid and for a better understanding of such effects.

3.5. Thermoelectric (TE) transport properties

Thermoelectric properties pertain to a material's capacity to transform heat into electrical energy. Thermoelectric devices fundamentally rely on this phenomenon to generate power, provide cooling, and measure temperature. To evaluate the appropriateness of a material for use in devices, it is essential to analyze various transport parameters, including electrical conductivity (σ), electronic thermal conductivity (k_e), Seebeck coefficient (S), power factor (PF), and the figure of merit (ZT).[68] The BoldTrap2 code is used to aid in this analysis, with a relaxation time of 10^{-14} s.[43] This approach assumes that the relaxation time, denoted as τ, remains constant and independent of temperature and carrier concentration, making the computations much easier. While this is a useful assumption in most theoretical studies, it may not be able to fully account for the complexities in the actual temperature-dependent scattering mechanisms in real materials. The calculations for all transport parameters are within the temperature range of 200–1000 K. Fig. 8(a)–(d) and 9(a)–(c) display the results of the thermoelectric parameters of the studied compounds as a function of temperature.

Fig. 8(a) illustrates the correlation between electrical conductivity and temperature which represents the material's ability to conduct an electric current. When the temperature rises, the electrical conductivity of Cs_2AuAsF_6/Cs_2AuSbF_6 exhibits a linear rise, ranging from $0.081/0.084 \times 10^{19}$ to $1.19/1.05 \times 10^{19}$ (Ω^{-1} m^{-1} s^{-1}). Higher temperatures eventually cause a stronger excitation of carriers across the band gap, which raises their conductivity. This is a common occurrence seen in semiconductors. At a temperature of 300 K, the electrical conductivity for Cs_2AuAsF_6 and Cs_2AuSbF_6 is 0.177×10^{19} and 0.175×10^{19} (Ω^{-1} m^{-1} s^{-1}), respectively, indicating a balanced charge transport capability in both compounds at room temperature. According to Fig. 8(b), when the carrier concentration (N) in a titled semiconductor increases, its electrical conductivity also increases due to the gain of more thermal energy of an electron, as follows:[69] $\sigma = Ne\mu$, where e and μ denote the electronic charge and mobility. This increase in electrical conductivity can lead to an enhancement in electronic thermal conductivity (k_e/τ) due to a proportionate relationship

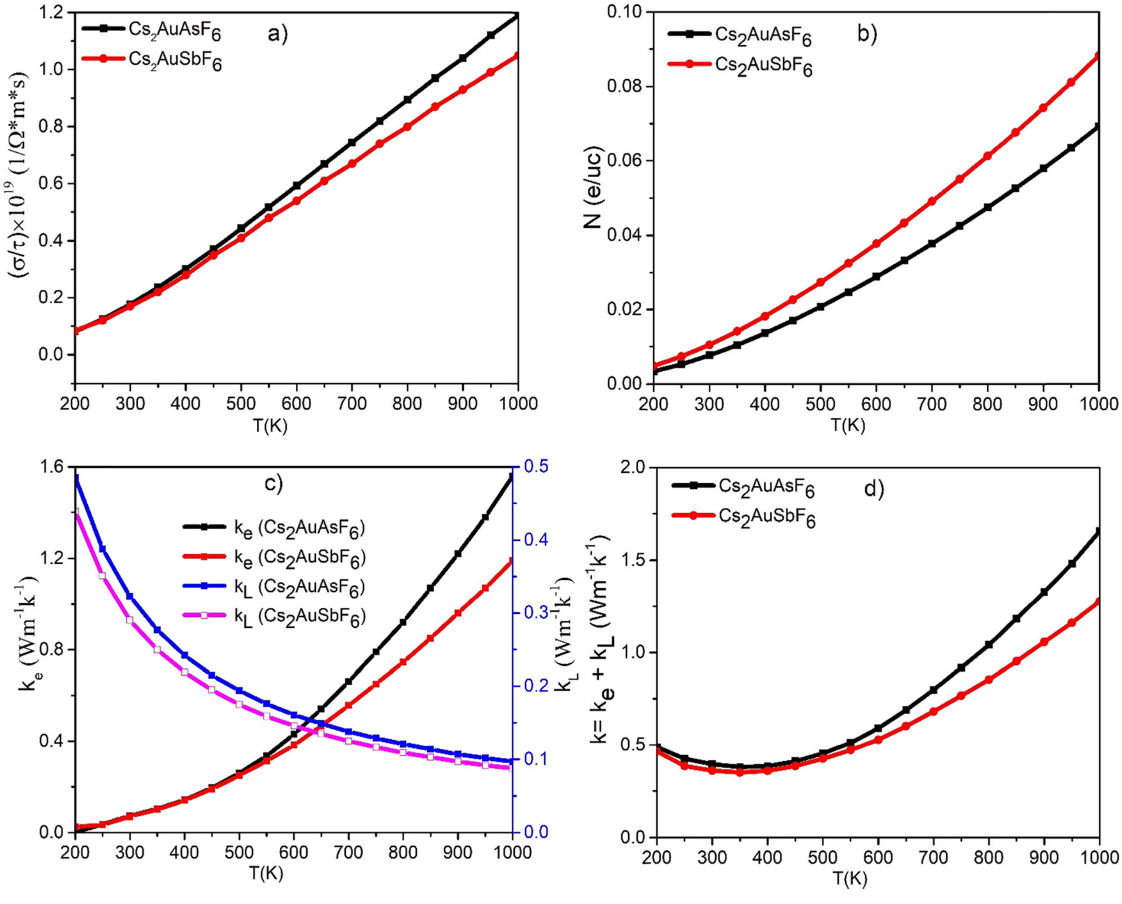

Fig. 8 (a) σ/τ: electrical conductivity, (b) N: carrier concentration, (c) k_e: electronic thermal conductivity; k_L: lattice thermal conductivity, and (d) k: total thermal conductivity.

among them, which supports the Wiedemann–Franz Law as follows:[70] $k_e = LT\sigma$, where L is the Lorentz constant and T is the absolute temperature. Regarding thermoelectric applications, there is some real significance to the rise in electrical conductivity with temperature and carrier concentration. Furthermore, high electrical conductivity improves the passage of heat energy throughout the material in addition to facilitating the quick movement of charges. This suggests that Cs_2AuAsF_6 and Cs_2AuSbF_6 compounds would be suitable options for applications like thermoelectric devices that call for steady charge and heat transfer. However, it should be mentioned that there is always a trade-off between thermal and electric conductivity when designing these materials for high-efficiency thermoelectric applications.

Thermal conductivity is another important property that quantifies the ability of a substance to conduct heat. The total thermal conductivity comprises two distinct components: the lattice component, resulting from vibrations in the lattice structure (k_L), and the electronic component (k_e), attributed to the movement of charge carriers.[71] As illustrated in Fig. 8(c), the value of the electronic thermal conductivity (k_e) of the investigated compounds increases with temperature. This trend indicates that increasing temperatures thermally excite more electrons thereby increasing charge-carrier mobility and facilitating heat transfer. The k_e values determined at room temperature (300 K) for Cs_2AuAsF_6 and Cs_2AuSbF_6 are 0.072 and 0.07 W m^{-1} K^{-1}, respectively. The temperature-dependent lattice thermal conductivity (k_L), which is derived from the Slack equation[72] (Fig. 8(c), ESI†), also demonstrates a clear inverse relationship between temperature and k_L values; as temperature increases, k_L values drop. The observed effect of k_L demonstrates that the transfer of heat by phonons reduces as the temperature rises. The lattice thermal conductivity k_L values for Cs_2AuAsF_6 and Cs_2AuSbF_6 at a temperature of 300 K are 0.323 and 0.29 W m^{-1} K^{-1}, respectively. Fig. 8(d) shows the total thermal energy transfer by phonons (k_L) and charge carriers (k_e), which varies with temperature. The low k_{total} ($k_{total} = k_L + k_e$) values, particularly in terms of k_L, which decreases further as the temperature rises, suggest that $Cs_2AuAsFa_6$ and Cs_2AuSbF_6 could be useful materials for limiting heat dissipation from the thermoelectric device and promoting the existence of a thermal gradient throughout the material. By restricting the transfer of heat through phonons and permitting sufficient conduction of heat through electrons, this imposition of balance between the lattice thermal conductivity and the electronic thermal conductivity enhances the potential thermoelectric performance and application of Cs_2AuAsF_6 and Cs_2AuSbF_6. These results imply that these materials might be able to work in energy conversion processes if their electrical and thermal characteristics are suitably improved.

This behavior of σ and κ_e increasing with the increase in temperature is generally expected in semiconductors due to increased carrier excitation attempting to reach thermal equilibrium. Nevertheless, these two factors have to be optimized so that the *ZT* value would be as high as possible. Higher temperature values of Cs_2AuSbF_6, for example, may provide an edge with slightly lower values of κ_L, hence maintaining the heat gradient essential for thermoelectric efficiency. Further improvement in thermoelectric efficiency could be sought with strategies such as doping or nano-structuring that may reduce κ_L but allow maintaining high σ, thus improving *ZT* values and making these materials more attractive for many applications.

The Seebeck coefficient (S) is an essential indicator for determining the dominant carriers in a compound and reflects the capability of the material to generate a voltage due to the presence of a temperature gradient. A positive value indicates the presence of holes, classifying the compound as a p-type semiconductor. Fig. 9(a) displays the relationship between the Seebeck coefficient and temperature. Furthermore, at room temperature (300 K), Cs_2AuAsF_6 has a higher Seebeck coefficient value (276 μV K^{-1}) than Cs_2AuSbF_6 (266 μV K^{-1}). The dispersion of the band gap near the Fermi level directly influences both the Seebeck coefficient and electrical conductivity, forming an inverse relationship.[73] The Seebeck coefficient also exhibits an inverse correlation with the concentration of charge carriers, as follows:[74]

$$S = \left(\frac{8\pi^2 k_B{}^2}{3h^2 e}\right)\left(\frac{\pi}{3N}\right)^{2/3} m^* T$$

The above relation suggests that S is directly linked with effective mass m^*. A high dispersion curve around the Fermi level indicates the existence of a low effective mass, which results in high mobility and a high Seebeck coefficient. When a material has a high S value—more than 250 μV K^{-1}—it is considered to be very effective for thermoelectric power generation.[75] Since a highly scattered band has a smaller effective mass and therefore better mobility of the charge carriers, which is advantageous for thermoelectric conversion, the thermoelectric performance is greatly dependent on the band dispersion near the Fermi level. In energy conversion applications like waste heat recovery and renewable energy sources, Cs_2AuAsF_6 and Cs_2AuSbF_6 are beneficial because of their high Seebeck coefficients, which generate high temperatures that allow them to produce voltage in the presence of temperature differentials.

The power factor (PF) is a direct measure of a material's ability to convert thermal energy into electrical energy efficiently. It provides a measure of the electrical performance of a material for thermoelectric applications, combining the Seebeck coefficient and electrical conductivity. The power factor is defined as PF = $S^2\sigma/\tau$. Fig. 9(b) shows that the power factor increases from 0.625 × 10^{11} W m^{-1} K^{-2} s^{-1} to 5.87 × 10^{11} W m^{-1} K^{-2} s^{-1} for Cs_2AuAsF_6 and 0.611 × 10^{11} W m^{-1} K^{-2} s^{-1} to 4.74 × 10^{11} W m^{-1} K^{-2} s^{-1} for Cs_2AuSbF_6 with the increase in temperature from 200 to 1000 K, respectively. The fact that PF rises with temperature implies that a favorable $S{-}\sigma$ balance causes both materials to perform better thermoelectrically as the temperature rises. Cs_2AuAsF_6 and Cs_2AuSbF_6 are potential candidates for high-temperature thermoelectric devices, where an efficient engine transfers heat to electricity, as indicated by the greater PF values at elevated temperatures.

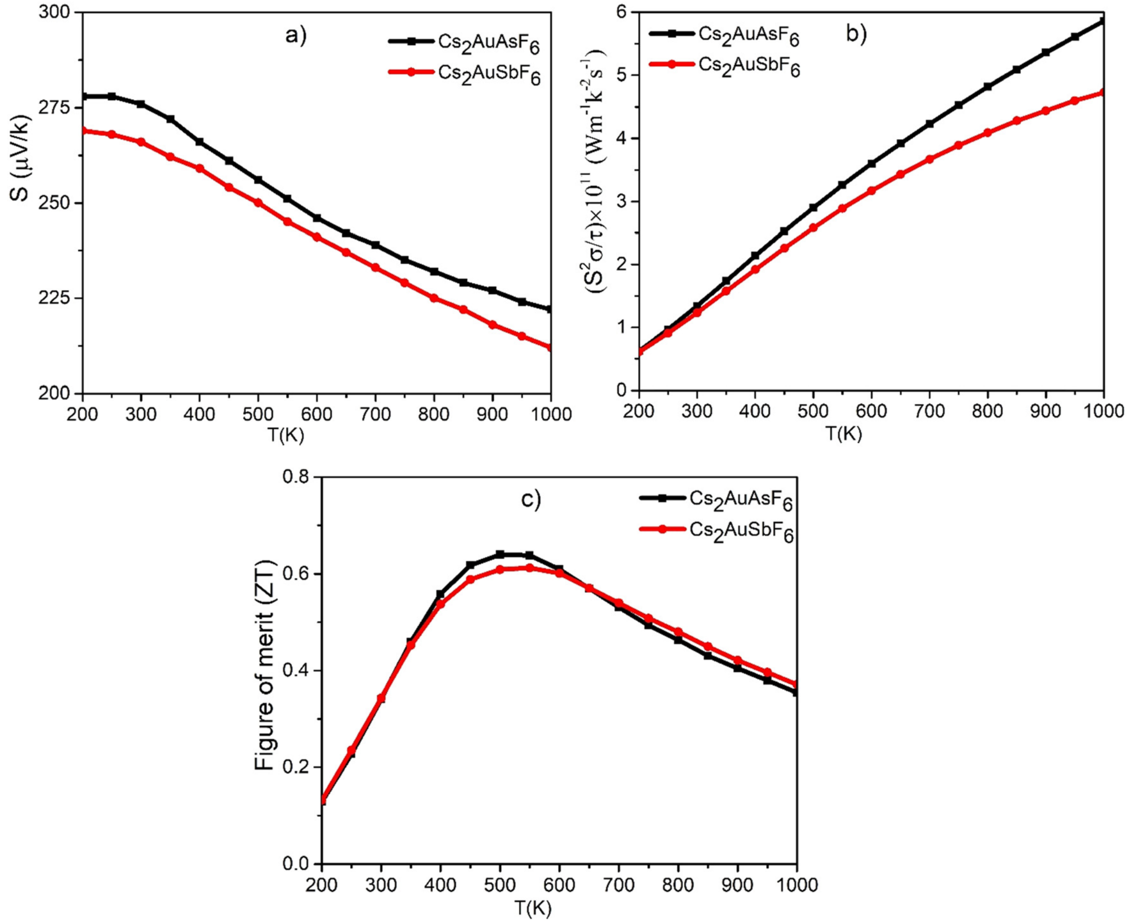

Fig. 9 (a) S: Seebeck coefficient, (b) $S^2\sigma/\tau$: power factor and (c) ZT: figure of merit of the studied compounds.

A dimensionless parameter that evaluates the efficiency of a thermoelectric material is the figure of merit (ZT). It is defined as[76] $ZT = \frac{S^2\sigma}{k}T$. To be considered the ideal choice of thermoelectric materials, ZT must be valued at one or greater. Furthermore, a higher ZT value can be attained by either increasing the value of the Seebeck coefficient and electrical conductivity or decreasing the thermal conductivity (k). Higher values indicate greater thermoelectric efficiency. The larger the magnitude of ZT, the higher the performance in energy conversion from heat to electricity. These effects (changing of S, σ and k) are shown in Fig. 9(c), which depicts ZT *versus* T, demonstrating an increase in ZT values as the temperature increases. This trend is most prevalent in semiconductors. The highest ZT value achieved for Cs_2AuAsF_6 within the temperature range of 500–550 K is 0.64, whereas the maximum value obtained for Cs_2AuSbF_6 within that temperature range is 0.61. Values near $ZT = 1$ are very impressive and generally preferred for waste heat recovery applications. Although these ZT values may be somewhat far from the ideal values of high-performance thermoelectric materials, the rather low thermal conductivities of the compounds, 0.32 and 0.29 W m^{-1} K^{-1}, offer moderate thermoelectric efficiency by limiting heat loss. Also, there is a consistent drop in the ZT values of the titled compounds as the temperature increases from 600 to 1000 K. Therefore, we anticipate that these double-halide perovskites under investigation could potentially serve as viable choices for heat management device applications in industrial processes.

Increased carrier scattering and reduced mobility at higher thermal energies contribute to the weakening temperature dependence of S and the plateauing of ZT at elevated temperatures. This signifies optimizing carrier concentration for obtaining high S values while maintaining reduced thermal losses. These are very useful observations because Cs_2AuAsF_6 and Cs_2AuSbF_6 were found appropriate for mid- to high-temperature thermoelectric devices such as recovery systems from industrial waste heat. Their moderate ZT values highlight the opportunity to introduce these materials in devices which will need efficient energy conversion in the temperature range mentioned. However, here the stability of ZT values up to 500 K places these materials as real contender candidates for applications demanding full-fledged thermoelectric behavior like automobile exhaust recovery or relevant industrial furnace environments.

Using the output of structural and electronic parameters as input parameters in the BoltzTraP2 code, thermoelectric parameters such as the Seebeck coefficient (S), electrical conductivity (σ), and electronic thermal conductivity (k_e) have been calculated for a range of chemical potentials. Variations in these parameters are graphically depicted in Fig. 10 and 11.

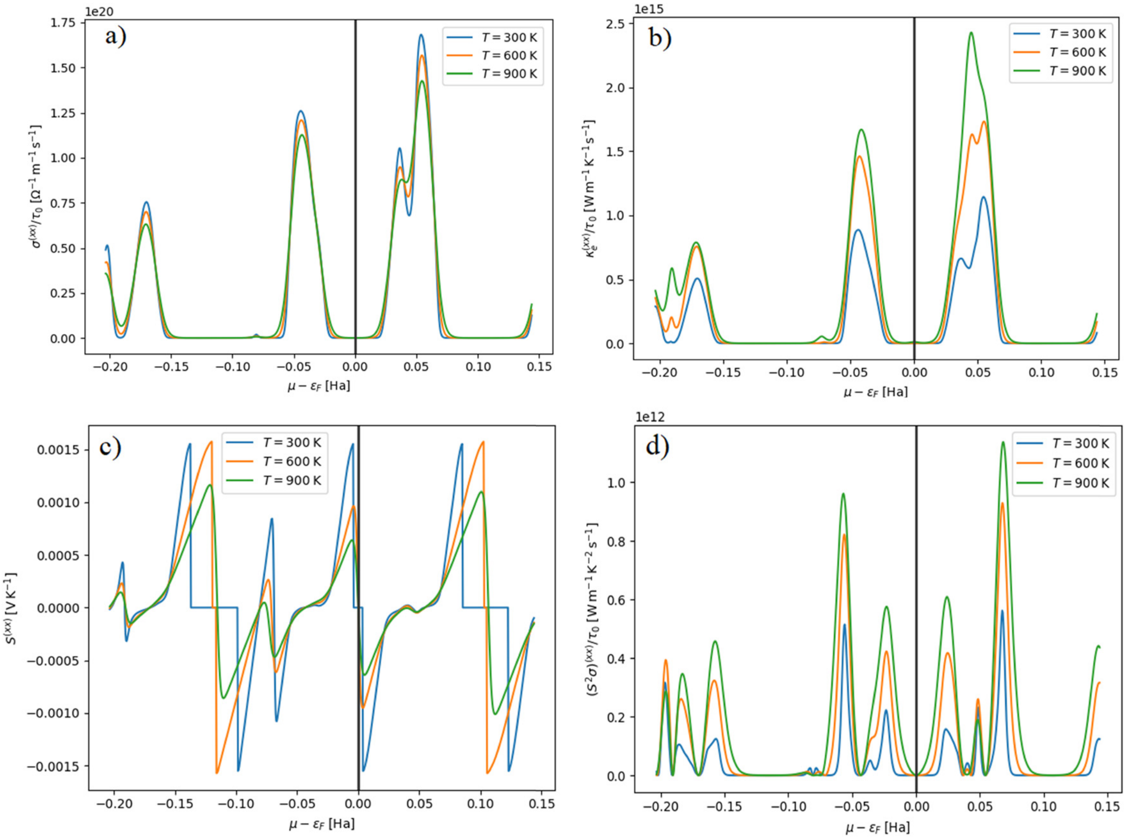

Fig. 10 (a) Electrical conductivity (σ), (b) electronic thermal conductivity (κ_e), (c) Seebeck coefficient (S) and (d) power factor against chemical potential for Cs_2AuAsF_6.

Concerning the thermal conductivity (k_e) and electrical conductivity (σ), which are calculated with the relaxation time, the code in question operates under the constant relaxation time approximation (CRTA = τ_0 = 10^{-14} s). However, in the CRTA context, the Seebeck coefficient (S) is strongly calculated independent of any tunable parameters. At 300, 600, and 900 K, Fig. 10(a) and 11(a) show the normalized electrical conductivity σ/τ_0 as a function of $\mu - \epsilon_f$ for Cs_2AuAsF_6 and Cs_2AuSbF_6, respectively. For Cs_2AuAsF_6, when conductivity peaks at certain $\mu - \epsilon_f$ values, the carriers function at highly mobile energy levels. These peaks widen as the temperature increases, suggesting more carrier dispersion. This trend highlights the temperature-dependent conductivity changes caused by the electronic band structure and phonon interactions of the material. Conductivity response shows a similar behavior for Cs_2AuSbF_6, which has distinct peaks that marginally alter as the temperature changes. These peaks are essentially related to the energy level at which mobility is greatest, generated by band structure characteristics. With the increase in temperature, the broadening of peaks results in an increase in scattering and dispersion of carriers. This is further corroborated by the thermal excitation of electrons. Cs_2AuSbF_6 shows slightly higher conductivity in a few regions making it better than Cs_2AuAsF_6 for utilization under conditions seeking high mobility of carriers. However, Cs_2AuSbF_6 is found to have somewhat higher conductivity in specific conductivity zones, which suggests that these compounds have different electronic structures, which could lead to variations in their thermoelectric figure of merit. Within the same temperature ranges, Fig. 10(b) and 11(b) shows the relationship between the dimensionless electronic thermal conductivity (κ_e/τ_0) and the parameter $\mu - \epsilon_f$. Both graphs show that the thermal conductivity peaks rise with temperature, suggesting that heat conduction improves with the mobility of the utilized carriers. The peak arises from the contribution of high-energy carriers for enhanced thermal conduction. The lower values of κ_e/τ_0 for Cs_2AuSbF_6 compared to Cs_2AuAsF_6 indicate that the former perhaps has a slight advantage in maintaining the thermal gradient which is beneficial for thermoelectric applications. There are limits to thermal and electrical transport that should be targeted for optimal performance, suggesting that the thermoelectric figure of merit for Cs_2AuAsF_6 may be hampered by the trend for higher thermal conductivity at higher temperatures because of increasing heat dissipation. In general, the thermal conductivity measurements of Cs_2AuSbF_6 are lower and still varied from one another. This could be because the crystals are arranged differently and the thermal phonon–electron interactions vary in such various structures. The Seebeck coefficient S throughout the chemical potential $\mu - \epsilon_f$ is depicted in Fig. 10(c) and 11(c). From the Cs_2AuAsF_6 graph, it was observed that the coefficient exhibits oscillating behavior, with the electron and hole contributions represented by the positive and negative peaks, respectively. Additionally, at higher temperatures, the

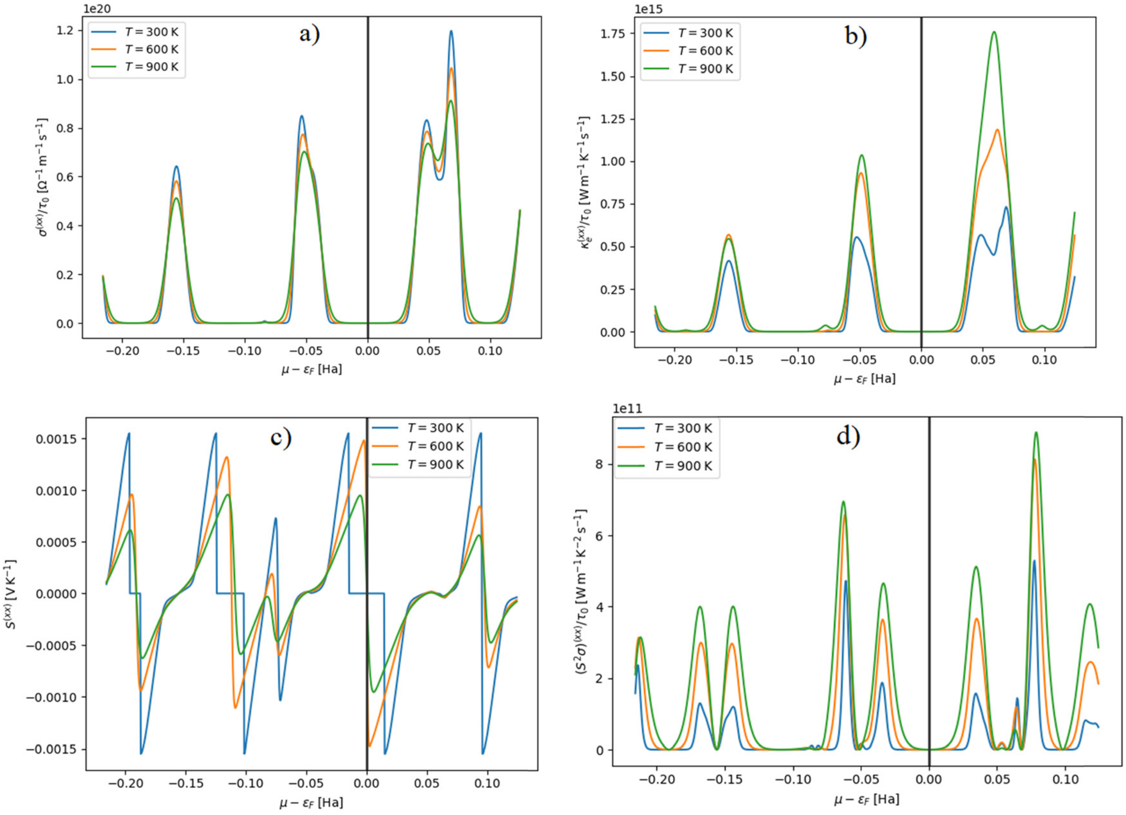

Fig. 11 (a) Electrical conductivity (σ), (b) electronic thermal conductivity (κ_e), (c) Seebeck coefficient (S) and (d) power factor against the chemical potential for Cs_2AuSbF_6.

oscillations tend to diminish, suggesting a reduced thermoelectric response that might be caused by phonon scattering. This implies that since carriers are unique, thermoelectric performance may be improved at higher temperatures. Although Cs_2AuSbF_6 exhibits the same rhythmic behavior, the amplitudes and precise locations of the peaks vary because of variations in atomic arrangement. These variations suggest that varied chemical potential values are needed to maximize thermoelectric efficiency in Cs_2AuSbF_6. In the case of Cs_2AuAsF_6, the Seebeck coefficient indicates more severe oscillations at lower temperatures, depicting that the compound has better thermoelectric performance in this regime. Moreover, the wider oscillations from Cs_2AuSbF_6 indicate a more uniform thermoelectric response across chemical potentials, which can benefit certain applications requiring stability over a wide operational use range. For different temperatures of 300 K, 600 K, and 900 K, Fig. 10(d) and 11(d) show how the power factor varies with $\mu - \epsilon_f$. The conductivity peaks, which increase with temperature and peak at 900 K, are correlated with the power factor peaks. This demonstrates that at high temperatures, thermoelectric performance improves. Since the conductivity and power factor peaks align, thermoelectric efficiency will be temperature-dependent in regions of high carrier mobility, making these materials suitable for high-temperature applications. In contrast to Cs_2AuAsF_6, the power factor has also shown peaks that resemble those of S and σ, albeit with somewhat different amplitudes and locations. High-temperature PF values of Cs_2AuAsF_6 suggest superior potential for thermoelectric applications compared with Cs_2AuSbF_6. Both compounds, however, have strong temperature dependence in their performance, qualifying them for high-temperature thermoelectric devices. This variant demonstrates how atomic arrangement affects thermoelectric performance and offers a chance to optimize $\mu - \epsilon_f$ for improved performance in Cs_2AuSbF_6.

It is noteworthy that the CRTA approach is not valid for phonon-limited scattering or the temperature- or carrier concentration-dependent relaxation time. A constant relaxation time of 10^{-14} s represents an over-simplification in this study, and so the calculated ZT values of 0.64 for Cs_2AuAsF_6 and 0.61 for Cs_2AuSbF_6 at 500 K should be regarded as approximations. To achieve more accurate predictions, more complex scattering models or experimental determination of relaxation times is required.

4. Conclusion

Within this study, we have conducted a comprehensive evaluation of the newly predicted lead-free double halide perovskites, $Cs_2Au^{I}M^{III}F_6$ (As, Sb), as material candidates capable of energy conversion with a special focus on photovoltaic energy harvesting and thermoelectric devices. Geometrically, these materials are confirmed to be cubic and stable, supported by negative formation energy, Goldschmidt's tolerance factor, and dynamic stability. In addition to the structural stability of $Cs_2AuM(As, Sb)F_6$, the assessment of mechanical stability based on Pugh's ratio, Poisson's ratio and Cauchy's pressure shows that these compounds are ductile which is fundamental for device fabrication and longevity. From the electronic structure viewpoint, both Cs_2AuAsF_6 and Cs_2AuSbF_6 contain indirect band gap regions of 1.144 eV and 1.746 eV respectively, obtained using the Tran-Blaha modified Becke–Johnson (TB-mBJ) method. Such band gap energies are appropriate for the active region of the visible range of light spectrum, where studies including optical ones also indicate that these materials possess high absorption coefficients (6.17×10^5 cm^{-1} for Cs_2AuAsF_6 and 5.17×10^5 cm^{-1} for Cs_2AuSbF_6) within the visible range as well. Such features reasonably classify them as efficient light harvesters making them suitable for implementation in solar cells. Besides, the low effective electron mass of the materials (0.16 for Cs_2AuAsF_6 and 0.25 for Cs_2AuSbF_6) contributes to enhanced electron mobility, thus supporting efficient charge separation and transport in a solar cell.

With the thermoelectric figure of merit *ZT* estimated using the Boltzmann transport theory, it is noted that these materials have moderate *ZT* values (0.64 for Cs_2AuAsF_6 and 0.61 for Cs_2AuSbF_6 at 500 K), showing that these materials may be relevant for thermoelectric applications such as industrial waste heat recovery. These materials show low lattice thermal conductivity which plays an important role in sustaining the temperature gradient, thereby increasing the thermoelectric efficiency. Even though these *ZT* values do not approach the upper limit of high-performance thermoelectric materials, they reflect a positive compromise between electrical and thermal conductivity rendering these perovskites suitable for real-world applications in thermoelectric devices operating at moderate temperature ranges.

All in all, the results we obtained demonstrate the applicability of $Cs_2Au^{I}M^{III}F_6$ (M = As, Sb) as eco-friendly substitutes for energy applications. Given their adjustable electronic and optical characteristics, as well as moderate thermoelectric efficiency and structural stability, they can be regarded as good materials for the provision of green and clean energy systems. Future work may be directed towards the experimental verification of these properties and searching for doped or alloyed forms of these substances with the aim of enhancing their efficiency in photovoltaic and thermoelectric systems. This study enhances the existing literature on lead-free perovskites which is critical in the making of new and safer materials for emerging energy systems.

Author's contribution

Shuaib Mahmud: writing – original draft, methodology, conceptualization, formal analysis, data calculations, validation. Usama Ahmed: writing – review & editing, methodology, formal analysis. Md. Atik Uz Zaman Atik: writing – original draft (partly), investigations, validation. Md. Mukter Hossain: writing – review & editing, validation. Md. Mohi Uddin: writing – review & editing, validation. Md. Ashraf Ali: conceptualization, formal analysis, validation, writing – review & editing, supervision, software.

Data availability

The data sets generated and/or analyzed in this study are available from the first/corresponding author on reasonable request.

Conflicts of interest

There are no conflicts to declare.

Acknowledgements

This work was carried out with the aid of a grant (grant number: 21-378 RG/PHYS/AS_G-FR3240319526) from UNESCO-TWAS and the Swedish International Development Co-operation Agency (SIDA). The views expressed herein do not necessarily represent those of UNESCO-TWAS, SIDA or their Board of Governors. **Shuaib Mahmud** expresses gratitude to the University Grants Commission (UGC) of Bangladesh for providing financial support to conduct the related research under Ph.D Fellowship program 2022–23.

References

1 H. Wang, M. Asif Amjad, N. Arshed, A. Mohamed, S. Ali and M. A. Haider Jafri, *et al.*, RETRACTED: Fossil Energy Demand and Economic Development in BRICS Countries, *Front. Energy Res.*, 2022, **10**, 842793.

2 C. Bogmans, L. Kiyasseh, A. Matsumoto and A. Pescatori, *Energy, Efficiency Gains and Economic Development: When Will Global Energy Demand Saturate?* (November 1, 2020), IMF Working Paper No. 20/253, Available at SSRN: https://ssrn.com/abstract=3758087.

3 W.-J. Yin, B. Weng, J. Ge, Q. Sun, Z. Li and Y. Yan, Oxide perovskites, double perovskites and derivatives for electrocatalysis, photocatalysis, and photovoltaics, *Energy Environ. Sci.*, 2019, **12**(2), 442–462.

4 P.-K. Kung, M.-H. Li, P.-Y. Lin, J.-Y. Jhang, M. Pantaler and D. C. Lupascu, *et al.*, Lead-free double perovskites for perovskite solar cells, *Sol RRL*, 2020, **4**(2), 1900306.

5 H. J. Snaith, Perovskites: the emergence of a new era for low-cost, high-efficiency solar cells, *J. Phys. Chem. Lett.*, 2013, **4**(21), 3623–3630.

6 Z. Deng, F. Wei, S. Sun, G. Kieslich, A. K. Cheetham and P. D. Bristowe, Exploring the properties of lead-free hybrid double perovskites using a combined computational-experimental approach, *J. Mater. Chem. A*, 2016, **4**(31), 12025–12029.

7 J. Haruyama, K. Sodeyama, L. Han and Y. Tateyama, First-principles study of ion diffusion in perovskite solar cell sensitizers, *J. Am. Chem. Soc.*, 2015, **137**(32), 10048–10051.

8 Y. Cai, W. Xie, H. Ding, Y. Chen, K. Thirumal and L. H. Wong, *et al.*, Computational study of halide perovskite-derived A_2BX_6 inorganic compounds: chemical trends in electronic structure and structural stability, *Chem. Mater.*, 2017, **29**(18), 7740–7749.

9 V. Kumar, A. Kathiravan and M. A. Jhonsi, Beyond lead halide perovskites: Crystal structure, bandgaps, photovoltaic properties and future stance of lead-free halide double perovskites, *Nano Energy*, 2024, **125**, 109523.

10 S. A. Dar and B. Want, Direct band gap double perovskite halide $Cs_2ScInCl_6$ for optoelectronic applications—A first principle study, *Comput. Condens. Matter*, 2022, **33**, e00736, DOI: **10.1016/j.cocom.2022.e00736**.

11 G. King and P. M. Woodward, Cation ordering in perovskites, *J. Mater. Chem.*, 2010, **20**(28), 5785–5796.

12 G. Volonakis, M. R. Filip, A. A. Haghighirad, N. Sakai, B. Wenger and H. J. Snaith, *et al.*, Lead-free halide double perovskites via heterovalent substitution of noble metals, *J. Phys. Chem. Lett.*, 2016, **7**(7), 1254–1259.

13 Q. Chen, N. De Marco, Y. M. Yang, T.-B. Song, C.-C. Chen and H. Zhao, *et al.*, Under the spotlight: The organic--inorganic hybrid halide perovskite for optoelectronic applications, *Nano Today*, 2015, **10**(3), 355–396.

14 A. H. Slavney, T. Hu, A. M. Lindenberg and H. I. Karunadasa, A bismuth-halide double perovskite with long carrier recombination lifetime for photovoltaic applications, *J. Am. Chem. Soc.*, 2016, **138**(7), 2138–2141.

15 E. T. McClure, M. R. Ball, W. Windl and P. M. Woodward, Cs_2AgBiX_6 (X = Br, Cl): new visible light absorbing, lead-free halide perovskite semiconductors, *Chem. Mater.*, 2016, **28**(5), 1348–1354.

16 L. Chu, W. Ahmad, W. Liu, J. Yang, R. Zhang and Y. Sun, *et al.*, Lead-free halide double perovskite materials: a new superstar toward green and stable optoelectronic applications, *Nano-Micro Lett.*, 2019, **11**, 1–18.

17 A. Bibi, I. Lee, Y. Nah, O. Allam, H. Kim and L. N. Quan, *et al.*, Lead-free halide double perovskites: Toward stable and sustainable optoelectronic devices, *Mater. Today*, 2021, **49**, 123–144.

18 X. Xu, Y. Zhong and Z. Shao, Double perovskites in catalysis, electrocatalysis, and photo (electro) catalysis, *Trends Chem.*, 2019, **1**(4), 410–424.

19 R. Hu, R. Ding, J. Chen, J. Hu and Y. Zhang, Preparation and catalytic activities of the novel double perovskite-type oxide La_2CuNiO_6 for methane combustion, *Catal. Commun.*, 2012, **21**, 38–41.

20 K. Radja, B. L. Farah, A. Ibrahim, D. Lamia, I. Fatima and B. Nabil, *et al.*, Investigation of structural, magneto-electronic, elastic, mechanical and thermoelectric properties of novel lead-free halide double perovskite $Cs_2AgFeCl_6$: first-principles calcuations, *J. Phys. Chem. Solids*, 2022, **167**, 110795.

21 S. Khawar, M. Q. Afzal, M. Husain, N. Sfina, H. Albalawi and M. A. Naeem, *et al.*, First-principles calculations to investigate structural, electronic, optical, and magnetic properties of a scintillating double perovskite halide ($Cs_2LiCeCl_6$), *J. Mater. Res. Technol.*, 2022, **21**, 4790–4798.

22 A. J. Kale, R. Chaurasiya and A. Dixit, Lead-Free $Cs_2BB'X_6$ (B: Ag/Au/Cu, B′: Bi/Sb/Tl, and X: Br/Cl/I) Double Perovskites and Their Potential in Energy Conversion Applications, *ACS Appl. Energy Mater.*, 2022, **5**(9), 10427–10445.

23 N. A. Noor, M. W. Iqbal, T. Zelai, A. Mahmood, H. M. Shaikh and S. M. Ramay, *et al.*, Analysis of direct band gap A_2ScInI_6 (A = Rb, Cs) double perovskite halides using DFT approach for renewable energy devices, *J. Mater. Res. Technol.*, 2021, **13**, 2491–2500.

24 Y. Cai, W. Xie, Y. T. Teng, P. C. Harikesh, B. Ghosh and P. Huck, *et al.*, High-throughput computational study of halide double perovskite inorganic compounds, *Chem. Mater.*, 2019, **31**(15), 5392–5401.

25 J. Li, L. Sun, X. Cao and J. Chang, First-Principles Predictions of Structural, Mechanical, and Optoelectronic Properties of Se-Based Double Perovskites A_2SeX_6 (A = Rb, K; X = Cl, Br, I), *J. Phys. Chem. C*, 2023, **127**(21), 10332–10340.

26 M. A. Ali, R. A. Alshgari, A. A. Awadh Bahajjaj and M. Sillanpää, The study of new double perovskites K_2AgAsX_6 (X = Cl, Br) for energy-based applications, *J. Taibah Univ. Sci.*, 2023, **17**(1), 2170680.

27 S. Mahmud, M. A. Ali, M. M. Hossain and M. M. Uddin, DFT aided prediction of phase stability, optoelectronic and thermoelectric properties of A_2AuScX_6 (A = Cs, Rb; X = Cl, Br, I) double perovskites for energy harvesting technology, *Vacuum*, 2023, 112926.

28 O. A. Lozhkina, A. A. Murashkina, M. S. Elizarov, V. V. Shilovskikh, A. A. Zolotarev and Y. V. Kapitonov, *et al.* Microstructural analysis and optical properties of $Cs_2BiAgBr_6$ halide double perovskite single crystals, *arXiv*, 2017, preprint, arXiv:171108148, DOI: **10.48550/arXiv.1711.08148**.

29 N. P. Mathew, N. R. Kumar and R. Radhakrishnan, First principle study of the structural and optoelectronic properties of direct bandgap double perovskite $Cs_2AgInCl_6$, *Mater. Today Proc.*, 2020, **33**, 1252–1256.

30 G. Nazir, Q. Mahmood, M. Hassan, M. M. AL-Anazy, N. A. Kattan and N. Sfina, *et al.*, Tuning of band gap by anions (Cl, Br, I) of double perovskites Rb_2AgAsX_6 (Cl, Br, I) for solar cells and thermoelectric applications, *Phys. Scr.*, 2023, **98**(2), 25811.

31 G. M. Mustafa, A. Slam, S. Saba, N. A. Noor, M. W. Iqbal and A. Dahshan, Optoelectronic and thermoelectric characteristics of halide based double perovskites K_2YAgX_6 (X = Br, I) for energy storage applications, *Polyhedron*, 2023, **229**, 116184.

32 A. Ayyaz, G. Murtaza, S. Alotaibi, S. Ali and I. Boukhris, Investigation of Promising Lead-Free Double Perovskites Rb_2TlBiZ_6 (Z = Cl, Br, and I) as Sustainable Alternatives for Photovoltaic and Wasted Heat Conversion Applications: First Principles Analysis, *J. Inorg. Organomet. Polym. Mater.*, 2024, 1–4.

33 S. Al-Qaisi, M. Mushtaq, S. Alomairy, T. V. Vu, H. Rached and B. U. Haq, *et al.*, First-principles investigations of Na_2CuMCl_6 (M = Bi, Sb) double perovskite semiconductors: materials for green technology, *Mater. Sci. Semicond. Process.*, 2022, **150**, 106947.

34 S. R. Bhandari, D. K. Yadav, B. P. Belbase, M. Zeeshan, B. Sadhukhan and D. P. Rai, *et al.*, Electronic, magnetic,

optical and thermoelectric properties of $Ca_2Cr_{1-x}Ni_xOsO_6$ double perovskites, *RSC Adv.*, 2020, **10**(27), 16179–16186.

35 S. Mahmud, M. M. Hossain, M. M. Uddin and M. A. Ali, Prediction of X_2AuYZ_6 (X = Cs, Rb; Z = Cl, Br, I) double halide perovskites for photovoltaic and wasted heat management device applications, *J. Phys. Chem. Solids*, 2025, **196**, 112298.

36 A. Boutramine, S. Al-Qaisi, S. Samah, A. K. Alqorashi, T. A. Alrebdi and M. Ezzeldien, *et al.*, First-principles Investigations of Structural, Thermodynamic, Optoelectronic and Thermoelectric Properties of Rb_2CuMF_6 (M = As^{3+}, Bi^{3+}) Eco-friendly Halide Double Perovskites: Materials for Green Energy Applications, *J. Inorg. Organomet. Polym. Mater.*, 2024, 1–18.

37 W. Kohn and L. J. Sham, Density functional theory, *Conference Proceedings-Italian Physical Society*, 1996, pp. 561–572.

38 K. Schwarz, DFT calculations of solids with LAPW and WIEN2k, *J. Solid State Chem.*, 2003, **176**(2), 319–328.

39 J. P. Perdew, K. Burke and M. Ernzerhof, Generalized gradient approximation made simple, *Phys. Rev. Lett.*, 1996, **77**(18), 3865.

40 H. Ehrenreich and M. H. Cohen, Self-consistent field approach to the many-electron problem, *Phys. Rev.*, 1959, **115**(4), 786–790.

41 F. Tran and P. Blaha, Accurate band gaps of semiconductors and insulators with a semilocal exchange-correlation potential, *Phys. Rev. Lett.*, 2009, **102**(22), 226401.

42 A. J. Hong, C. L. Yuan and J. M. Liu, Quaternary compounds Ag_2XYSe_4 (X = Ba, Sr; Y = Sn, Ge) as novel potential thermoelectric materials, *J. Phys. D: Appl. Phys.*, 2020, **53**(11), 115302.

43 G. K. H. Madsen, J. Carrete and M. J. Verstraete, BoltzTraP2, a program for interpolating band structures and calculating semi-classical transport coefficients, *Comput. Phys. Commun.*, 2018, **231**, 140–145Available from:.

44 M. Jamal, M. Bilal, I. Ahmad and S. Jalali-Asadabadi, IRelast package, *J. Alloys Compd.*, 2018, **735**, 569–579.

45 S. J. Clark, M. D. Segall, C. J. Pickard, P. J. Hasnip, M. I. J. Probert and K. Refson, *et al.*, First principles methods using CASTEP, *Z. Kristallogr. - Cryst. Mater.*, 2005, **220**(5–6), 567–570.

46 S.-Q. Sun, Y. Cai, M. Zhu, W. He, B.-C. Liu and Y.-L. Xu, *et al.*, Highly Efficient Hybrid Perovskite/Organic Tandem White Light Emitting-Diodes with External Quantum Efficiency Exceeding 20%, *Adv. Funct. Mater.*, 2023, **33**(51), 2306549.

47 V. G. Tyuterev and N. Vast, Murnaghan's equation of state for the electronic ground state energy, *Comput. Mater. Sci.*, 2006, **38**(2), 350–353.

48 Y. Fu, M. P. Hautzinger, Z. Luo, F. Wang, D. Pan and M. M. Aristov, *et al.*, Incorporating large A cations into lead iodide perovskite cages: Relaxed goldschmidt tolerance factor and impact on exciton--phonon interaction, *ACS Cent. Sci.*, 2019, **5**(8), 1377–1386.

49 W. Travis, E. N. K. Glover, H. Bronstein, D. O. Scanlon and R. G. Palgrave, On the application of the tolerance factor to inorganic and hybrid halide perovskites: a revised system, *Chem. Sci.*, 2016, **7**(7), 4548–4556.

50 C. J. Bartel, C. Sutton, B. R. Goldsmith, R. Ouyang, C. B. Musgrave and L. M. Ghiringhelli, *et al.*, New tolerance factor to predict the stability of perovskite oxides and halides, *Sci. Adv.*, 2019, **5**(2), eaav0693Available from:.

51 R. D. Shannon, Revised effective ionic radii and systematic studies of interatomic distances in halides and chalcogenides, *Acta Crystallogr., Sect. A*, 1976, **32**(5), 751–767.

52 A. E. Fedorovskiy, N. A. Drigo and M. K. Nazeeruddin, The role of Goldschmidt's tolerance factor in the formation of A_2BX_6 double halide perovskites and its optimal range. Small, *Methods*, 2020, **4**(5), 1900426.

53 C. Li, X. Lu, W. Ding, L. Feng, Y. Gao and Z. Guo, Formability of abx3 (x = f, cl, br, i) halide perovskites, *Acta Crystallogr., Sect. B: Struct. Sci.*, 2008, **64**(6), 702–707.

54 S. Nair, M. Deshpande, V. Shah, S. Ghaisas and S. Jadkar, Cs_2TlBiI_6: a new lead-free halide double perovskite with direct band gap, *J. Phys.: Condens. Matter*, 2019, **31**(44), 445902.

55 S. Maqsood, G. Murtaza, N. A. Noor, R. Neffati, S. Nazir and A. Laref, First-principle investigation of thermoelectric and optoelectronic properties of Rb_2KScI_6 and Cs_2KScI_6 double perovskite for solar cell devices, *J. Mater. Res. Technol.*, 2022, **21**, 841–849Available from.

56 G. Giorgi, J.-I. Fujisawa, H. Segawa and K. Yamashita, Small photocarrier effective masses featuring ambipolar transport in methylammonium lead iodide perovskite: a density functional analysis, *J. Phys. Chem. Lett.*, 2013, **4**(24), 4213–4216.

57 G. C. La Rocca, Wannier–Mott Excitons in Semiconductors, *Electronic Excitations in Organic Nanostructures*, Academic Press, 2003, pp. 97–128. Thin Films and Nanostructures; vol. 31. Available from: https://www.sciencedirect.com/science/article/pii/S1079405003310026.

58 M. Wuttig, C.-F. Schön, M. Schumacher, J. Robertson, P. Golub and E. Bousquet, *et al.*, Halide perovskites: advanced photovoltaic materials empowered by a unique bonding mechanism, *Adv. Funct. Mater.*, 2022, **32**(2), 2110166.

59 T. Saha, M. M. H. Babu, M. Arifuzzaman and J. Podder, Thermodynamic and dynamic stability in a new potential $Cs_2AgAsCl_6$ perovskite: insight from DFT study, *Phys. Chem. Chem. Phys.*, 2022, **24**(43), 26609–26621.

60 C. Ambrosch-Draxl and J. O. Sofo, Linear optical properties of solids within the full-potential linearized augmented planewave method, *Comput. Phys. Commun.*, 2006, **175**(1), 1–14.

61 V. K. Rashenov, M. G. Foigel and R. A. Alarashi, Dielectric Function of a Model Semiconductor, *Phys. Status Solidi*, 1972, **54**(1), 355–368.

62 D. R. Penn, Wave-number-dependent dielectric function of semiconductors, *Phys. Rev.*, 1962, **128**(5), 2093.

63 M. K. Butt, M. Yaseen, I. A. Bhatti, J. Iqbal, A. Murtaza and M. Iqbal, *et al.*, A DFT study of structural, magnetic, elastic and optoelectronic properties of lanthanide based $XAlO_3$ (X = Nd, Gd) compounds, *J. Mater. Res. Technol.*, 2020, **9**(6), 16488–16496.

64 H. H. Hegazy, G. M. Mustafa, A. Nawaz, N. A. Noor, A. Dahshan and I. Boukhris, Tuning of direct bandgap of Rb_2ScTlX_6(X = Cl, Br, I) double perovskites through halide

ion substitution for solar cell devices, *J. Mater. Res. Technol.*, 2022, **19**, 1271–1281, DOI: 10.1016/j.jmrt.2022.05.082.

65 A. El Amrani, A. Bekhtari, A. El Kechai, H. Menari, L. Mahiou and M. Maoudj, *et al.*, Determination of the suitable refractive index of solar cells silicon nitride, *Superlattices Microstruct.*, 2014, **73**, 224–231Available from: https://www.sciencedirect.com/science/article/pii/S0749603614001840.

66 P. R. Varadwaj and H. M. Marques, Physical and optoelectronic features of lead-free $A_2AgRhBr_6$ (A = Cs, Rb, K, Na, Li) with halide double perovskite composition, *J. Mater. Chem. C*, 2020, **8**(37), 12968–12983.

67 J. Xie, F. Liu and K. Yan, Perovskite Solar Cells Processed by Solution Nanotechnology, in *Advanced Nanomaterials for Solar Cells and Light Emitting Diodes*, ed. F. Gao, Elsevier, 2019, ch. 5, pp. 119–174. (Micro and Nano Technologies). Available from: https://www.sciencedirect.com/science/article/pii/B9780128136478000059.

68 T. J. Scheidemantel, C. Ambrosch-Draxl, T. Thonhauser, J. V. Badding and J. O. Sofo, Transport coefficients from first-principles calculations, *Phys. Rev. B: Condens. Matter Mater. Phys.*, 2003, **68**(12), 125210.

69 K. Kaur and R. Kumar, Effect of pressure on electronic and thermoelectric properties of magnesium silicide: a density functional theory study, *Chin. Phys. B*, 2016, **25**(5), 56401.

70 W. Kim, Strategies for engineering phonon transport in thermoelectrics, *J. Mater. Chem. C*, 2015, **3**(40), 10336–10348.

71 J. P. Heremans, V. Jovovic, E. S. Toberer, A. Saramat, K. Kurosaki, A. Charoenphakdee, S. Yamanaka and G. J. Snyder, Enhancement of thermoelectric efficiency in PbTe by distortion of the electronic density of states, *Science*, 2008, **321**(5888), 554–557.

72 G. A. Slack, The thermal conductivity of nonmetallic crystals, *Solid State Phys.*, 1979, **34**, 1–71.

73 D. Narducci, E. Selezneva, G. Cerofolini, S. Frabboni and G. Ottaviani, Impact of energy filtering and carrier localization on the thermoelectric properties of granular semiconductors, *J. Solid State Chem.*, 2012, **193**, 19–25.

74 X. Zhang and L.-D. Zhao, Thermoelectric materials: Energy conversion between heat and electricity, *J. Mater.*, 2015, **1**(2), 92–105.

75 K. Kutorasinski, B. Wiendlocha, S. Kaprzyk and J. Tobola, Electronic structure and thermoelectric properties of n-and p-type SnSe from first-principles calculations, *Phys. Rev. B: Condens. Matter Mater. Phys.*, 2015, **91**(20 205201.

76 F. J. DiSalvo, Thermoelectric cooling and power generation, *Science*, 1999, **285**(5428), 703–706.